2-2013

Crystalline cellulose elastic modulus predicted by atomistic models of uniform deformation and nanoscale indentation

Xiawa Wu
Birck Nanotechnology Center, Purdue University, xiawa.wu@gmail.com

Robert J. Moon
Birck Nanotechnology Center, Purdue University; United States Forest Service, rmoon@purdue.edu

Ashlie Martini
University of California - Merced

Wu, Xiawa; Moon, Robert J.; and Martini, Ashlie, "Crystalline cellulose elastic modulus predicted by atomistic models of uniform deformation and nanoscale indentation" (2013). *Birck and NCN Publications.* Paper 1339.
http://dx.doi.org/10.1007/s10570-012-9823-0

Cellulose (2013) 20:43–55
DOI 10.1007/s10570-012-9823-0

ORIGINAL PAPER

Crystalline cellulose elastic modulus predicted by atomistic models of uniform deformation and nanoscale indentation

Xiawa Wu · Robert J. Moon · Ashlie Martini

Received: 7 July 2012 / Accepted: 9 November 2012 / Published online: 30 November 2012

Abstract The elastic modulus of cellulose $I\beta$ in the axial and transverse directions was obtained from atomistic simulations using both the standard uniform deformation approach and a complementary approach based on nanoscale indentation. This allowed comparisons between the methods and closer connectivity to experimental measurement techniques. A reactive force field was used that explicitly describes hydrogen bond, coulombic and van der Waals interactions, allowing each contribution to the inter- and intramolecular forces to be analyzed as a function of crystallographic direction. The uniform deformation studies showed that the forces dominating elastic behavior differed in the axial and transverse directions because of the relationship between the direction of the applied strain and the hydrogen bonding planes. Simulations of nanoscale indentation were then introduced to model the interaction between a hemispherical indenter with the $(1\bar{1}0)$ surface of a cellulose Iβ rod. The role of indenter size, loading force and indentation speed on the transverse elastic modulus was studied and, for optimized parameters, the results found to be in good agreement with experimentally-measured transverse elastic modulus for individual cellulose crystals.

Keywords Elastic modulus · Nanoindentation · Cellulose · Molecular dynamics

X. Wu (✉)
School of Mechanical Engineering, Purdue University, West Lafayette, IN, USA
e-mail: wu123@purdue.edu

R. J. Moon
Forest Products Laboratory, US Forest Service, Madison, WI, USA
e-mail: robertmoon@fs.fed.us

R. J. Moon
Birck Nanotechnology Center and the School of Material Engineering, Purdue University, West Lafayette, IN, USA

A. Martini
School of Engineering, University of California Merced, Merced, CA, USA
e-mail: amartini@ucmerced.edu

Introduction

With a growing demand for products made from renewable and sustainable resources, cellulose nanomaterials are increasingly being used to develop a variety of composite materials (Postek et al. 2008). Cellulose nanocrystals (CNCs) are whisker-like nanoparticles (typically 3–20 nm wide by 50–4,000 nm in length) of crystalline cellulose extracted from cellulose microfibrils by acid hydrolysis (Moon et al. 2011; Samir et al. 2005). Understanding the structure and mechanics of crystalline cellulose (Iβ) and how this relates to the properties of CNCs at a fundamental level can facilitate development of CNC composites as

well as broaden our general knowledge of CNC behavior as a nanomaterial.

The elastic modulus of CNCs is an important mechanical property, not only from a potential composite application perspective, but because it provides a means of linking experimental measurements to modeling results so that the validity of model predictions can be assessed. Due to the structural anisotropy within crystalline cellulose (i.e. non symmetric: crystal structure, cellulose chain structure, and cellulose chain arrangement within the crystal structure), mechanical properties will be dependent on the direction relative to the cellulose crystalline structure. The elastic modulus of crystalline cellulose and CNCs in the axial (E_A) and transverse (E_T) directions measured experimentally using various methods and predicted by simulation has recently been reviewed (Moon et al. 2011) and is summarized in Table 1. Note that the transverse elastic moduli are considered collectively (i.e. all transverse orientations perpendicular to chain direction). The wide distribution in the reported experimental values comes about primarily from differences in measurement techniques and the materials tested (i.e. different percent crystallinity, etc). For simulations the wide distribution comes about as a result of differences in model parameters (simulation method, configuration of the modeled structure, atomic interaction models, etc), and the method of calculating elastic modulus (Moon et al. 2011).

Molecular dynamics simulation of cellulose Iβ has also been used to predict the role of hydrogen bonding

Table 1 Elastic modulus reported from simulation-based (Iβ only) and experimental studies

Material	E_A (GPa)	E_T (GPa)	Experimental technique/model force filed	Reference
Experiment				
Cellulose fibrils	120–138	–	X-ray diffraction (XRD)	Sakurada et al. (1962)
				Sakurada et al. (1964)
				Matsuo et al. (1990)
				Diddens et al. (2008)
Cellulose fibrils	220 ± 50	15 ± 1	Inelastic X-ray scattering (IXS)	Diddens et al. (2008)
CNC-plant	105	–	Raman	Rusli and Eichhorn (2008)
CNC-wood	–	18–50	AFM indentation—FEA	Lahiji et al. (2010)
CNC-Tunicate	143	–	Raman	Sturcová et al. (2005)
CNC-Tunicate	151 ± 29	–	AFM-3pt bend	Iwamoto et al. (2009)
CNC-Tunicate	–	2–25	AFM indentation	Wagner et al. (2010), Wagner et al. (2011)
				Postek et al. (2011)
CNC-wood	–	24.8 ± 7.0	AFM indentation—FEA	Pakzad et al. (2012)
CNC-cotton	–	17.7 ± 5.0	AFM indentation—FEA	Pakzad et al. (2012)
Modeling				
Single chain	168	11–50	Dreiding	Tashiro and Kobayashi (1991)
Single chain	145	–	COMPASS	Sturcová et al. (2005)
1 × 1 × 1 unit cell	149	18–47	COMPASS	Eichhorn and Davies (2006)
1 × 1 × 1 unit cell	148	–	CHARMM	Reiling and Brickmann (1995)
1 × 1 × 1 unit cell	111	–	COMPASS	Tanaka and Iwata (2006)
3 × 3 × 2 unit cell	136	–	GROMOS	Kroon-Batenburg and Kroon (1997)
3 × 3 × 2 unit cell	115	–	Custom	Neyertz et al. (2000)
4 × 4 × 10 unit cell	125	–	COMPASS	Tanaka and Iwata (2006)
4 × 4 × 8 unit cell	156	–	GROMOS	Bergenstråle et al. (2007)

E_A = Elastic modulus in the axial direction, E_T = Elastic modulus in transverse direction

on crystalline stability and properties (Eichhorn and Davies 2006). The hydrogen bonding is relatively strong along the chain axis (intra-chain) and is well characterized, however, there is less consensus as to the inter-chain hydrogen bonding as it is difficult to quantify (Nishiyama 2009; Nishiyama et al. 2008). The intra- and inter-chain hydrogen bonding is most prevalent within the (200) plane, named the "hydrogen-bonded" plane (Fig. 1), and the existence of two coexisting hydrogen bonding systems has been proposed (Nishiyama 2009; Nishiyama et al. 2008). The hydrogen bonding within planes (110) and $(1\bar{1}0)$ is substantially lower and attractive van der Waals forces are considered to dominate the cohesion (Nishiyama et al. 2003; Cousins and Brown 1995). The ability to correctly describe these forces is critical to accurately modelling the $I\beta$ structure and properties.

In this study, atomistic simulations are used to predict the elastic properties of cellulose $I\beta$ in both the axial and transverse directions using two distinct methods: uniform deformation and nanoscale indentation. The former is used to validate the model by comparison to reported experiment and simulation based data in the literature, and results are analyzed in terms of variation in the multiple contributions to force and energy during the deformation process. An interatomic force field is used that explicitly describe hydrogen, coulombic and van der Waals bonding, allowing the study of these forces on the Iβ elastic properties. A nanoscale indentation model is then introduced to directly link atomic force microscopy (AFM) indentation experiments to atomistic simulations. This approach provides not only new validation methods for model predictions, but can be used to assess model parameters associated with different types of bonding within and between the multiple cellulose $I\beta$ lattice planes.

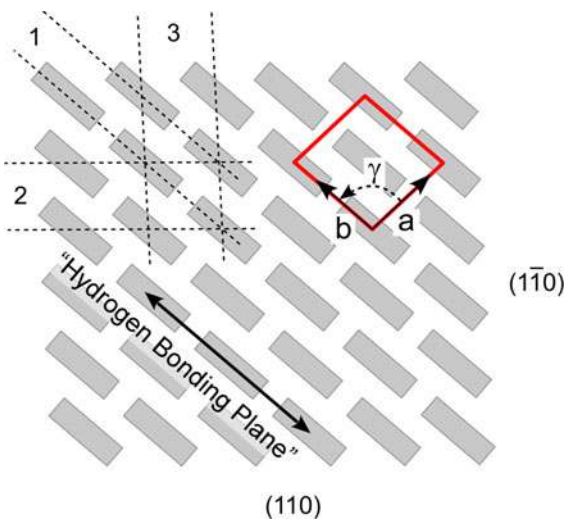

Fig. 1 Schematic of an idealized wood CNC cross-section along the cellulose chain-axis direction (i.e. the *c*-axis), showing terminating surfaces [(110) and $(1\bar{1}0)$] and the $I\beta$ unit cell projection superimposed on the crystal lattice (Moon et al. 2011). The three major lattice planes, (200), (110), and $(1\bar{1}0)$, have d-spacings of 0.39, 0.53, and 0.61 nm, respectively, which are labeled 1, 2 and 3. Each *grey box* represents a cellulose chain looking down the chain-axis

Methodology

Atomistic model

A model cellulose $I\beta$ crystal was constructed using Materials Studio commercial software based on the latest experimental diffraction results with unit cell parameters: $a = 7.784$ Å, $b = 8.201$ Å, $c = 10.380$ Å (chain direction), $\alpha = \beta = 90°$, and $\gamma = 96.5°$ (Nishiyama et al. 2002). The ReaxFF forcefield (Mattsson et al. 2010) was used to describe all interatomic interactions. This model provides accurate description of bond breaking and bond formation because atomic connectivity is determined using bond orders calculated from interatomic distances during the simulation. The model also accounts for non-bonded interactions such as van der Waals and coulombic, and it has an explicit expression for hydrogen bonds (a separate term in the energy formulation). Two simulations approaches were taken, uniform deformation and nanoscale indentation, both using LAMMPS modeling software.

Uniform deformation

For uniform deformation studies, a cellulose $I\beta$ crystal was constructed by expanding the unit cell four times in the *a* and *b* directions and eight times in the *c* direction. A snapshot of the simulation cell illustrating these dimensions is given in Fig. 2. The *c* dimensional length of the crystals was chosen based on previous research of a single cellulose chain subject to axial deformation which showed that a minimum chain

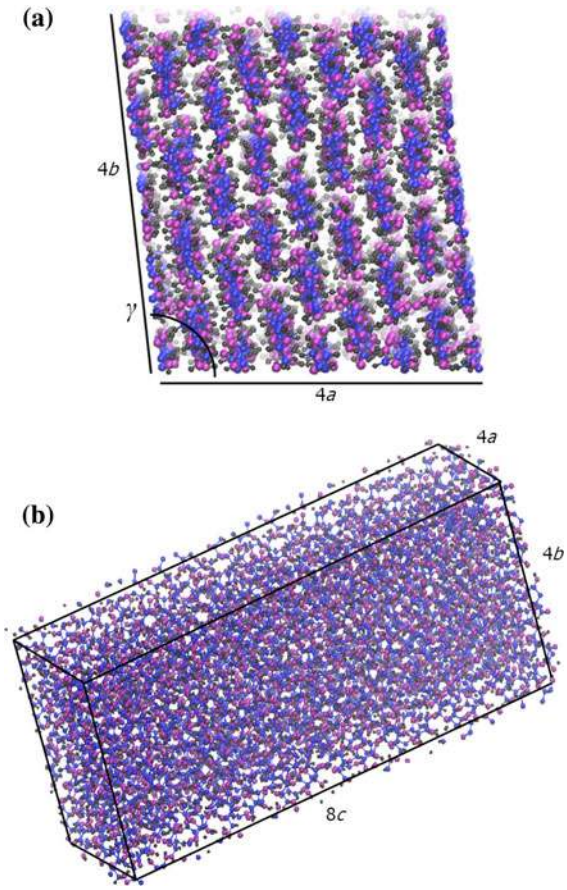

Fig. 2 Snapshots of the atomistic cellulose *Iβ* model used for simulations of uniform deformation: **a** is the a-b cross-section and, **b** is the 3-dimentiaon cellulose crystal. Atoms are represented as *spheres*: *blue*–carbon, *purple*–oxygen, and *black*–hydrogen (*sphere size* not representative of atomic dimensions)

length was required for repeatability in predicted properties (Wu et al. 2011). Note that we use the notation *a*, *b* and *c* to describe the directions of displacements and forces (as opposed to a set of orthogonal axes *x*, *y*, *z*) throughout this paper. For uniform deformation simulations, periodic boundary conditions were applied in all directions to model the bulk material.

The crystal was first equilibrated in the NVT ensemble (constant number of atoms, volume and temperature) for 20 ps at a temperature of 300 K to relax the inner stress of the initial configuration without changing its overall crystal parameters. Then it was equilibrated in the NPT ensemble (constant number of atoms, pressure and temperature) for 700 ps at 300 K and a pressure of 1 atm. During this process, both the inner stress and the stress enforced by the simulation cell boundaries were relaxed such that the dimensions of the crystal could vary. Finally, an energy minimization simulation was performed using the conjugate gradient algorithm such that, after equilibrium, the system was in a stable and energy minimum state. The unit cell parameters after equilibration and energy minimization were: $a = 8.549$ Å, $b = 8.922$ Å, $c = 10.814$ Å, $\alpha = \beta = 90°$, and $\gamma = 99.8°$. The initial side lengths were ≈ 86, ≈ 32 and ≈ 34 Å in the *c*, *a* and *b* directions, respectively.

Uniform deformation was performed using molecular mechanics. First, axial deformation was applied by stretching the simulation domain in the *c* direction in increments of 0.16 Å while *a* and *b* directions were controlled so that the total volume of the system was unchanged. This volume control method employed a default Poisson's ratio of ~ 0.5, which is an assumed value that provides an upper bound to the elasticity behavior. Energy minimization was performed after each deformation increment. The stress tensor at each step was recorded together with the axial length. The axial elastic modulus was then calculated as the ratio of the stress to the strain in the *c*-direction. Transverse uniform deformation simulations were performed using the same procedure, but stretching the simulation domain in either *a* or *b* direction with an increment of 0.06 Å. The maximum deformation applied in any one direction was less than 5 %. Investigating deformations in the three directions independently offers the most structural anisotropy, which should provide a contrast in the predicted elastic moduli.

Nanoscale indentation

For the nanoscale indentation simulations, the $(1\bar{1}0)$ surface of the crystal was created with periodic boundary condition in the axial-c direction and free boundaries in the other two directions, producing effectively a cellulose *Iβ* rod having a thickness of approximately 50 Å (seven cellulose chain layers), and a width of about 84 Å, as shown in Fig. 3. The $(1\bar{1}0)$ was considered here as one of the planes that will be a terminating surface for CNCs extracted from wood, plant and tunicate cellulose sources (Moon et al. 2011). The rod surface was modified by neutralizing any bonds broken during creation of the

surface with hydrogen atoms. The bottommost cellulose molecules were fixed to maintain structural rigidity.

A virtual rigid hemispherical indenter was used to indent the cellulose $I\beta$ rod such that the indentation was on the $(1\bar{1}0)$ plane in the $[1\bar{1}0]$ direction. The system was equilibrated at a temperature of 300 K for 10 ps prior to indentation. Initially, the lowest point of the indenter was 5 Å above the crystal surface. Then the indenter was brought down towards the surface at a constant speed V to simulate the indentation loading process. Once the indenter moved a certain depth into the surface, the unloading process was simulated by bringing the indenter up away from the surface at the same speed until the indenter returned to its original position. It is important to note that indentation speed in atomistic simulations is typically much larger than in an AFM experiments because speeds must be fast enough for the entire process to be modeled during the nanosecond-scale simulation duration (duration is limited to $\sim$ns because time step size is limited to $\sim$fs).

Indentation force–distance (F–d) curves were used to calculate the elastic modulus in the transverse directions. The force between the indenter and the substrate material was calculated by summing all forces normal to the surface exerted on the substrate atoms by the indenter using the formula

$$F(r) = -K(r-R)^2, \quad r < R, \tag{1a}$$

$$= 0, \quad r \geq R, \tag{1b}$$

where K is a force constant that controls the atom-indenter interaction force, r is the distance from an atom in the substrate to the center of the indenter, and R is the radius of the indenter. The indentation distance (d) was calculated by measuring the distance from the surface of the cellulose $I\beta$ substrate to the lowest position of the indenter. A positive value of d means the indenter is pressed into the substrate, while a negative value of d occurs when indenter and substrate are separated from each other.

The loading process usually is a combination of plastic and elastic processes, while unloading is

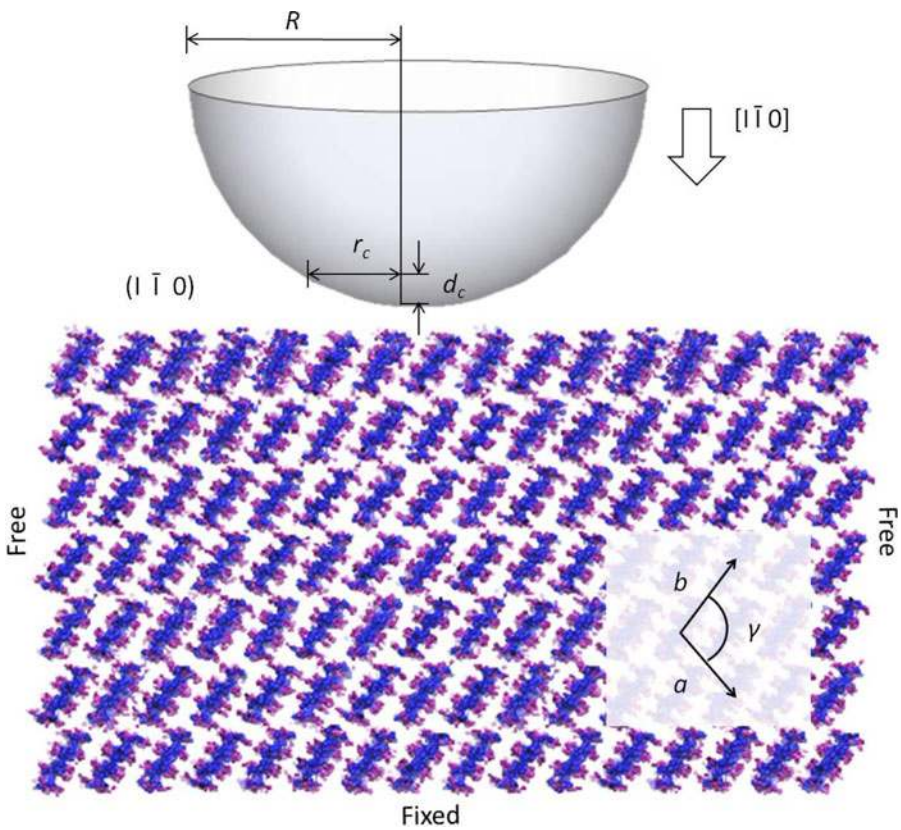

Fig. 3 Schematic of the simulation domain for nanoscale indentation simulations that is composed of a cellulose $I\beta$ film with hemispherical nanoscale indenter. The *bottom* of the thin film is fixed, while the other two dimensions have periodic boundary conditions. The R is the radius of the indenter, r_c is the radius of projected contact area, and d_c is the actual contact depth. The indentation surface is $(1\bar{1}0)$. The unit cell dimensions a, b and angle γ are identified on the figure

predominantly elastic. The F–d curves obtained from unloading were used for the elastic modulus calculation with the method presented by Oliver and Pharr (Oliver and Pharr 1992). Simulation data from the first non-zero force point to 95 % of the maximum loading distance was fit to the power function

$$F = a(d - d_f)^{3/2}, \tag{2}$$

where a and d_f are fitting parameters. Note that in experiments, the first approximately 5 % of the unloading data are not used for model fitting because of variability in the measurements, while in simulation, this data is not used because of the abrupt force changes. The contact stiffness (S) is the slope of the F–d unloading curve at the 95 % maximum loading point ($d_0 = 95\ \%d_{max}$).

$$S = \frac{d(F)}{d(d)} = \frac{3}{2}a(d - d_f)^{1/2} \tag{3}$$

at $d = d_0$. The contact depth (d_c) is determined by

$$d_c = d_0 - \theta\frac{F_0}{S}, \tag{4}$$

where $\theta = 0.75$ for a spherical indenter, and F_0 is the force at indentation distance d_0 during the unloading process. A reduced modulus (E_r) is related to the contact stiffness by

$$S = \frac{2\sqrt{A}}{\sqrt{\pi}}E_r, \tag{5}$$

where A is the projected contact area, calculated by

$$A = \pi r_c^2, \tag{6}$$

where r_c is the radius of projected contact area,

$$r_c = \sqrt{R^2 - (R - d_c)^2}. \tag{7}$$

Then, since the modulus of the indenter is infinitely large, i.e. $E_i = \infty$, the substrate material's elastic modulus (E_s) is

$$E_s = (1 - \nu_s^2)E_r, \tag{8}$$

where ν_s is Poisson's ratio (taken to be 0.5 consistent with the uniform deformation method). The hardness of the material (H) is calculated by

$$H = \frac{F_0}{A}. \tag{9}$$

Both elastic modulus and hardness have units of GPa.

Results and discussion

Uniform deformation

The predicted elastic moduli resulting from the uniform deformation studies are shown in the first column of Table 2, where each value is the average of five independent simulation trails. The predicted elastic modulus for both the axial and transverse directions is within the range of reported simulation and experimental data (see Table 1). As expected, the anisotropy in the cellulose $I\beta$ crystal results in different predicted elastic moduli in the axial and transverse directions. The elastic modulus in the axial c-direction is much larger than either transverse directions (a and b), while the elastic modulus in the b-direction was somewhat larger than that in the a-direction.

Role of anisotropy

To assess the mechanisms that contribute to the predicted elastic modulus anisotropy within cellulose $I\beta$, it is convenient to evaluate and compare the change in the force distribution during uniform deformation in the a direction [100], the b direction [010], and the c direction [001]. The total force of the system is a result of contributions from covalent bonds, covalent bond angles and torsion, van der Waals interactions (used generally here to refer to the Lennard-Jones force), coulombic (electrostatic) interactions, and hydrogen bonding. Figure 4 illustrates the distribution of attractive and repulsive forces involved for deformation in the c-direction (Fig. 4a), a-direction (Fig. 4b), and b-direction (Fig. 4c). This analysis reveals that the major attractive and repulsive forces during deformation differ between the three different orientations and likely account for the anisotropy in predicted elastic moduli.

For deformation in the c-direction the major attractive forces are due to covalent bonding and the angles between those bonds. This is reasonable since, in this orientation, elongation occurs along the length of individual cellulose chains where the covalent bonds between atoms in each chain will resist the deformation via an attractive force that attempts to bring both the atoms closer to one another and the bonds back to their equilibrium length. The dominant repulsive forces are van der Waals and coulombic.

Table 2 Elastic modulus (in units of GPa) of the model cellulose $I\beta$ crystal in each of the three coordinate directions calculated from uniform deformation simulations with hydrogen bonding turned "on" and "off"; averages and standard deviations obtained from five independent trials

Direction	Hydrogen bond "on"	Hydrogen bond "off"	Previous experiments (Table 1)	Previous simulations (Table 1)
c-axial	139.5 ± 3.5	120.3 ± 3.7	105–270	111–168
a-transverse	7.0 ± 1.7	9.5 ± 2.2	2–50	11–50
b-transverse	28.8 ± 2.9	12.6 ± 4.2		

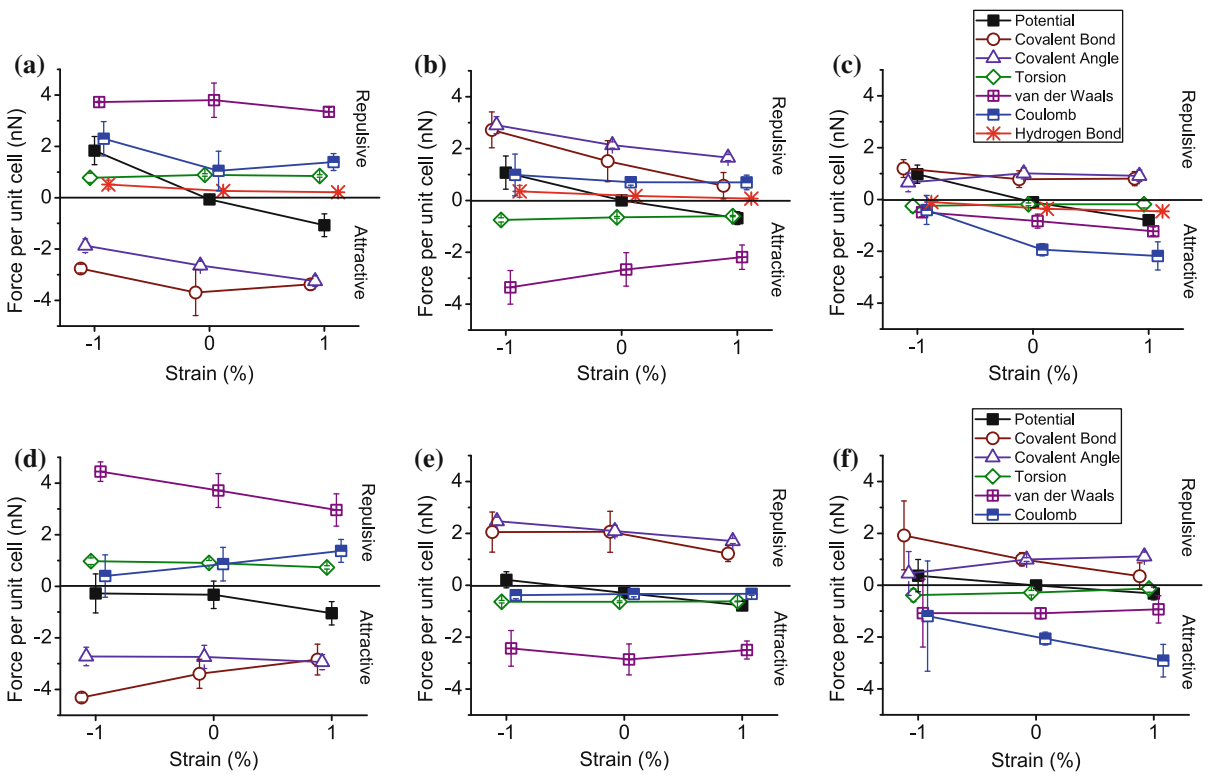

Fig. 4 **a–c** Change of the various force contributions in the *c* (axial), *a* and *b* directions, respectively. **d–f** Change of the various force contributions without hydrogen bonds in the *same directions*. Results are averages and standard deviations obtained from five independent trials

This again is reasonable since elongation in the chain direction causes neighboring chains to move closer together through Poisson contraction which in turn results in a larger repulsive force between atoms that are closer than they would be at equilibrium.

The variation of each energetic contribution during deformation in the *a* direction is shown in Fig. 4b. In this case the major repulsive forces are due to covalent bonds and bond angles, while the dominant attractive force is van der Waals. This is in agreement with previous literature showing that attractive van der Waals forces dominate the cohesion between (200) planes (i.e. the so called hydrogen bonding planes) (Kroon-Batenburg and Kroon 1997; Neyertz et al. 2000). During elongation, the space between planes is enlarged and the non-bonded force are attractive as they attempt to hold the planes together. Due to the Poisson effect, the other two directions, *c* and *b*, are compressed which cause repulsive covalent bond forces and non-negligible repulsive forces due to hydrogen bonding.

The force variation during deformation in the *b* direction is shown in Fig. 4c. As with the *a* direction, the most significant repulsive forces are due to covalent bonds and bond angles, while the dominant attractive forces are van der Waals and coulombic.

Additionally, there is a weak attractive force due to hydrogen bonding, which comes about from the deformation being within the hydrogen bonding planes. The hydrogen bonding plane (200) has the highest concentration of intra-chain (within a single cellulose chain) and inter-chain (between cellulose chains) hydrogen bonding (Reiling and Brickmann 1995; Tanaka and Iwata 2006) and displacement in the *b*-direction results in deformation within this plane (i.e. the [010] direction). As the displacement in the *b*-direction increases, both the intra-chain and inter-chain hydrogen bonds within the hydrogen bonding plane are stretched which results in an attractive restoring force.

Role of hydrogen bonding

To assess the role of intra- and inter- chain hydrogen bonding on the predicted elastic modulus in the *a*, *b*, and *c* directions, simulations were rerun with the hydrogen bonding effect turned "off". Results are shown in the second column of Table 2. The removal of hydrogen bonding had a negligible effect in the *a*-direction while it resulted in a decrease of the elastic modulus in *b* and *c* directions of approximately 16 and 19 GPa, respectively. This can again be understood through a force analysis. Figure 4d–f illustrate the variation in the force contributions during uniform deformation with hydrogen bonds "off". In the *c*-direction all forces change (compare Fig. 4a to 4d) to compensate for the lack of hydrogen bonding force, and the overall effect is a decrease in the magnitude of the axial elastic modulus ($\sim$14 %). A similar effect can be observed in the *b*-direction (compare Fig. 4c to 4f) where hydrogen bond removal caused a decrease in the elastic modulus ($\sim$56 %). The forces in the *a*-direction also change due to the removal of hydrogen bonds (compare Fig. 4b to 4e). However, there is a negligible change in elastic modulus in this direction.

These simulations have shown that removal of the hydrogen bonding decreases the elastic modulus in the *c*-direction (i.e. along the c-axis of cellulose $I\beta$), which is in agreement with the results of Eichhorn and Davies (2006) who report a decrease of approximately 25 GPa with the removal of hydrogen bonds. Although the trend is similar, there are differences between these two models; namely the forcefield in the previous work was COMPASS, while we employ ReaxFF in this study. This different is significant because COMPASS describes hydrogen bonds using the formulations for the electrostatic and van der Waals energies while ReaxFF has an explicit expression for the hydrogen bond calculation. Therefore, to turn "off" hydrogen bonding in COMPASS the electrostatic charge on the hydrogen atoms is set to zero (Eichhorn and Davies 2006). This method effectively removes hydrogen bonds from the simulation but may also affect the overall coulombic energy. As a result, there is no way to determine whether the observed decrease of axial elastic modulus is due to lack of hydrogen bonds or a coulombic effect. With ReaxFF's explicit treatment of hydrogen bond, we can turn "off" the hydrogen bond by setting a zero cutoff distance which means that the hydrogen bonds are removed without affecting atomic charges.

To further examine hydrogen bonding it is possible to compare the force due to hydrogen bonding and the number of hydrogen bonds per unit cell during deformation (Fig. 5a). A hydrogen bond is identified using distance and angle criteria of 3.5 Å and 30°, respectively. The results show that the number of hydrogen bonds per unit cell increases from 5.3 to nearly 6.1 during deformation. This can be analyzed by considering that, generally speaking, there are three types of hydrogen bonds in a cellulose $I\beta$ crystal: intra-chain, inter-chain within the hydrogen bonding plane, and inter-chain between two adjacent hydrogen bonding planes. Investigation of a single simulation case using Visual Molecular Dynamics software revealed that there are $\sim$2 intra-chain hydrogen bonds, $\sim$2 inter-chain hydrogen bonds within the hydrogen bonding plane, and $\sim$1 inter-chain hydrogen bonds between two adjacent hydrogen bonding planes per unit cell. During deformation (stretching) in the *a* direction, the number of inter-chain hydrogen bonds between two adjacent hydrogen bonding planes decreases, while there is an increase in the number of intra-chain and inter-chain hydrogen bonds within the hydrogen bonding plane; the result is an overall increase in number of hydrogen bonds per unit cell as shown in Fig. 5b. In contrast, for deformation (stretching) in the *b* direction, the number of inter-chain hydrogen bonds between two adjacent hydrogen bonding planes increases, while there is a decrease in the number of intra-chain and inter-chain hydrogen bonds within the hydrogen bonding plane; the overall effect is a decrease in number of hydrogen bonds per unit cell as shown in Fig. 5c.

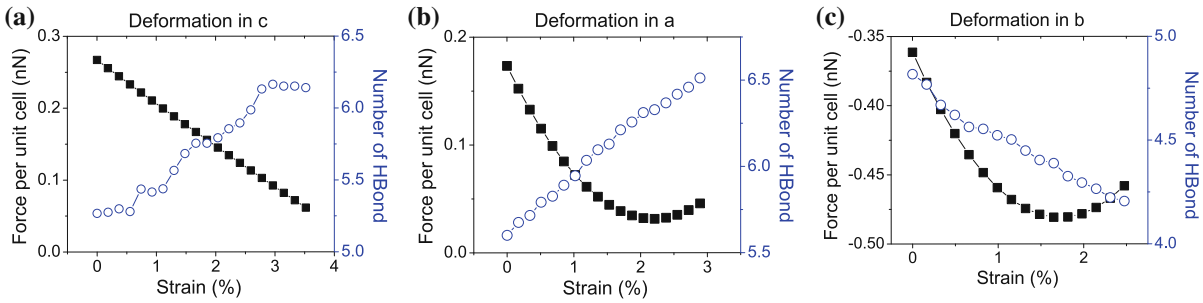

Fig. 5 **a–c** The hydrogen bond force (*square*) and number per unit cell (*circle*) during uniform deformation (stretching) in the *c* (axial), *a* and *b* directions, respectively. Results are averaging over five independent trials

Note that, for deformations (stretching) in the *a* and *b* directions, the overall changes in the number of hydrogen bonds per unit cell have opposite effects on force: the hydrogen bond force is positive (repulsive) in Fig. 5b and negative (attractive) in Fig. 5c. However, it is important to recognize that the hydrogen bond force is a quantity that reflects the strength of all hydrogen bonds, not just the number that exist. Indeed, the energy of a given hydrogen bond can vary significantly depending on the relative positions of the component atoms. Hydrogen bonds are very hard to experimentally characterize and there is still debate as to the specific role of hydrogen bonding within cellulose structures. The intention of this analysis is not to make any claims as to the hydrogen bonding structure or density, but rather to explore the possibilities of how changes in hydrogen bonding could occur as a function of deformation in different directions. We have presented the number of hydrogen bonds here only as a reference; quantification of the relationship between bond count, atomic configuration, and energy requires a more detailed study that is beyond the scope of this research. Nonetheless, this study demonstrates the elusive behavior of hydrogen bonding and that considerable work will be necessary to fully understand its role in the properties of crystalline cellulose.

Nanoscale indentation

The transverse elastic modulus and hardness were calculated by modeling nanoscale indentation on the cellulose $I\beta(1\bar{1}0)$ surface as described in "Nanoscale indentation" section. The results of this calculation are determined by model parameters that must be chosen prior to the simulation. In this work, we examined some of those parameters that most significantly affect the elastic modulus: indenter size, force constant and indentation speed. Indenter size was characterized by its radius, R, and we consider three values, 25, 50, and 75 Å. The second parameter was the force constant, K (see Eq. 1), which we varied from $K = 0.1$ kcal/mole-Å^3 (0.00695 nN/Å^2) to $K = 10.0$ kcal/mole-Å^3 (0.695 nN/Å^2). The third parameter was indentation speed, ranging from $V = 10$–1,000 m/s.

Figure 6a shows the effect of the indenter's radius on the F–d curve for $K = 0.1$ kcal/mole-Å^3 and indentation speed $V = 50$ m/s. The indenter radius is one of the most important parameters in nanoscale indentation because it will change the projected contact area and the resulting effective strain profile beneath the indenter (smaller indenter results in larger strain profiles for a given indentation depth), which affects the transverse elastic modulus and hardness. For a penetration depth of $d_0 = 9.45$ Å the projected contact area of the small indenter (Area = 824 Å^2) was much smaller than that of the large indenter (Area = 3,008 Å^2), and appears to have a minor effect on the measured properties (Fig. 6b); statistically these differences were found to be insignificant. Scanning electron microscopy (SEM) images of an AFM tip before and after indentation showed the radius to be $\sim 100 \pm 20$ Å (Wagner et al. 2011). However, with indentation depth on the order of 10 Å, it is realistic to expect local asperities on the AFM tip would effectively reduce the "true" contact tip radius. Therefore, we assume model tip radius of $R = 50$ Å or larger is a reasonable estimation.

The effect of force constant K on the F–d curves is shown in Fig. 7a for $R = 50$ Å and $V = 50$ m/s. As expected, the larger force constant results in a non-negligible interaction force at shallower indentation

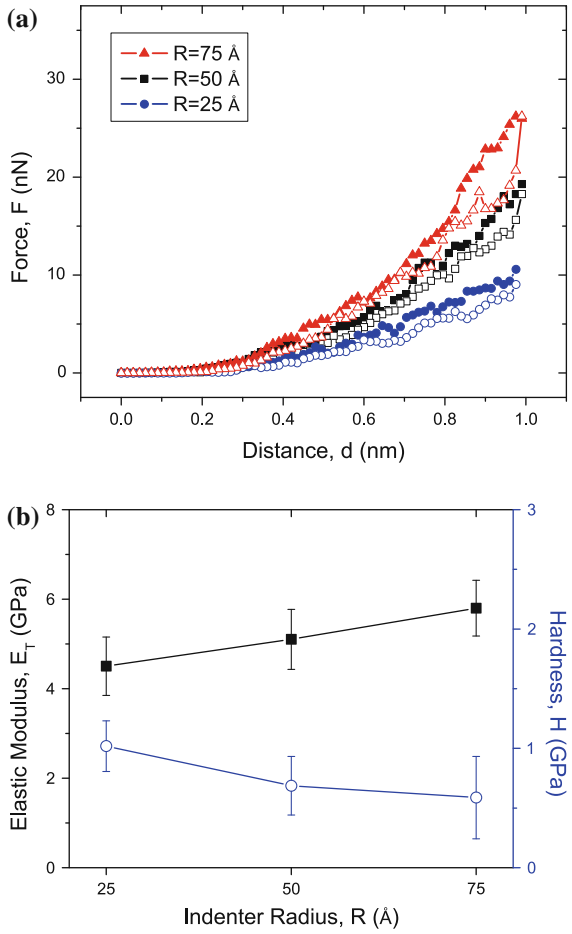

Fig. 6 **a** Force–distance (F–d) curves from the loading (*solid shapes*) and unloading (*hollow shapes*) process for three model AFM tip radii R with a force constant $K = 0.1$ kcal/mole-Å^3 and indentation speed $V = 50$ m/s, and **b** corresponding transverse elastic modulus (*square*) and hardness (*circle*). Results are averages and standard deviations obtained from five independent trials

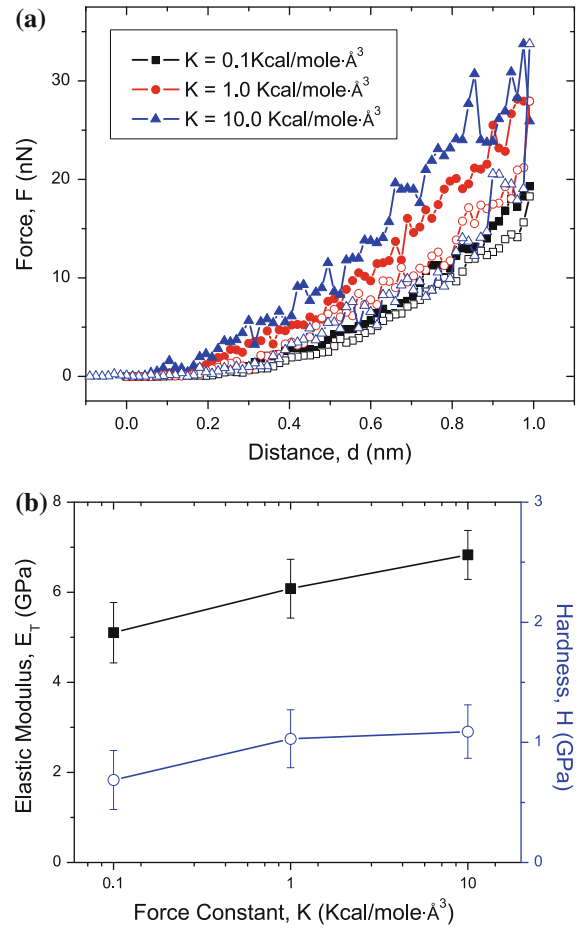

Fig. 7 **a** Force–distance curves during loading (*solid shapes*) and unloading (*hollow shapes*) using three different force constants K for a simulation with $R = 50$ Å and indentation speed $V = 50$ m/s, and **b** corresponding transverse elastic modulus (*square*) and hardness (*circle*). Results are averages and standard deviations obtained from five independent trials

depths and a greater maximum indentation force. However, Fig. 7b shows that increasing this constant causes a minimal increase in the elastic modulus and hardness. The force constant used in simulations cannot be directly compared to an experimentally defined parameter because we are only modeling the apex of an AFM tip, which is necessarily much smaller and less massive than the complete physical system. However, we identified $K = 0.1$ kcal/mole-Å^3 to be a reasonable value since it corresponds to a maximum force (total interaction force between tip and substrate) within the experimental loading force range of $F_{max} = 10$–30 nN given in (Wagner et al. 2011).

Indentation speed is a factor that cannot be compared directly between simulation and experiments. As mentioned previously, model indentation speed is necessarily higher than in experiment to enable a reasonable simulation duration. As shown in Fig. 8a, simulations were run at speeds ranging from 10 to 1,000 m/s. This parameter appears to have a more significant effect than K or R. Figure 8b illustrates that both the elastic modulus and hardness in transverse direction increase with indentation speed. However, it can be observed that, in the speed range $V = 10$–100 m/s, the modulus and hardness remain relatively constant. Therefore, to obtain a good balance between accuracy and computational efficiency, an indentation speed of $V = 50$ m/s was chosen.

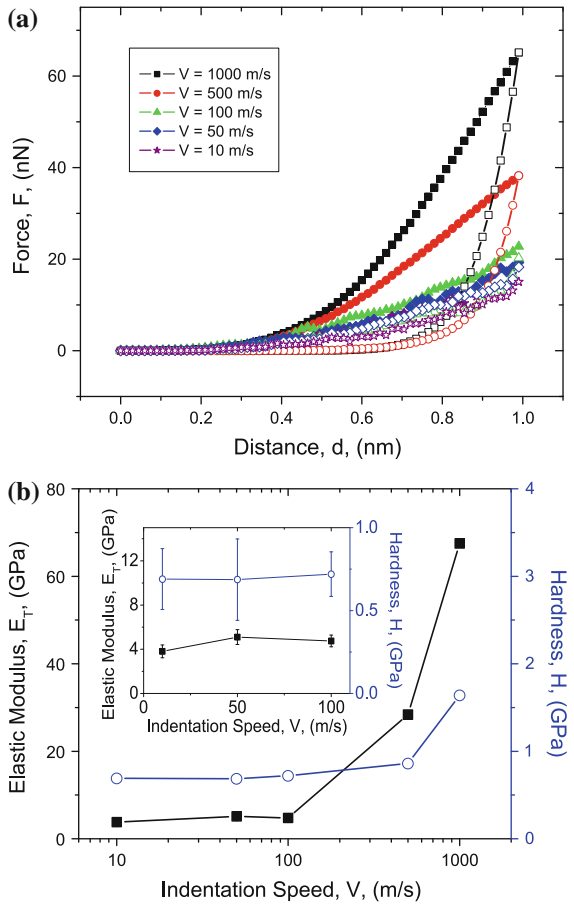

Fig. 8 **a** Force–distance curves during loading (*solid shapes*) and unloading (*hollow shapes*) using five different indentation speeds V for a simulation with $R = 50$ Å and force constant $K = 0.1$ kcal/mole-Å^3, and **b** corresponding transverse elastic modulus (*square*) and hardness (*circle*). Results are averages and standard deviations obtained from five independent trials

The preferred parameters identified above ($V = 50$ m/s, $K = 0.1$ kcal/mole-Å^3 and $R = 50$ Å) were used to generate F–d data and fit to the power law formula given in Eq. 2. The resulting elastic modulus was $E_T = 5.1 \pm 0.7$ GPa and the hardness was $H = 0.7 \pm 0.3$ GPa, both averages and standard deviations obtained from five independent simulations. This E_T is reasonable in comparison to experimental nanoscale indentation measurements performed by Wagner et al. (2011) who reported the elastic modulus of an isolated cellulose crystal to have a mean value of 8.1 GPa and a 95 % confidence interval of 2.7–20 GPa (based on 85 indents along Tunicate crystal). Finally, using a statistical analysis we found that the effects of radius, force constant and speed (in the range 10–100 m/s) on the predicted elastic modulus in the transverse direction were statistically insignificant; these parameters considered both individually and in combinations can be said to have no effect on the elastic modulus in transverse direction with a 95 % confidence interval.

A closer examination of the nanoindentation model shows that a potential edge effect should also be considered (Jakes et al. 2008, 2009; McAllister et al. 2012). The Oliver and Pharr (Oliver and Pharr 1992) method we used for nanoindentation calculation assumes the test material is homogeneous, filling a half-space and has a rigid support at the bottom. Since the rod-like shape model is finite (i.e. is not a half-space), edge effects may be significant. In fact, we observed that performing the simulation using a rod that was half the width of the original decreased both the transverse elastic modulus and the hardness. Visual analysis of the narrow rod simulation revealed that the surface chains were being pushed aside during the indentation process suggesting that the edge effects should be considered. However, a detailed analysis is beyond the scope of this paper.

Conclusion

The elastic modulus and hardness of a cellulose Iβ crystal were studied using uniform deformation and nanoscale indentation methods via atomistic simulation. The uniform deformation method predicted elastic modulus by measuring the crystal's response to uniaxial strain in each of the three crystallographic directions. The elastic modulus in the c, a and b directions was found to be 139.5 ± 3.5, 7.0 ± 1.7 and 28.8 ± 2.9 GPa, respectively, all of which are within the range of previous experimental and simulation results. Further analysis of the various energetic contributions, including hydrogen bonding, in the three directions revealed different deformation mechanisms which corresponds to the dependency of the elastic modulus on orientation.

Simulations of nanoscale indentation described the interaction between a hemispherical indenter with the $(1\bar{1}0)$ surface of a cellulose Iβ rod. Three major factors—indenter size, loading force and indentation speed—were examined in terms of their effect on the transverse elastic modulus and hardness. It was shown that the indenter's size and the loading force had little

effect on the results in the tested range. The indentation speed had little effect as well for speeds in the range of 10–100 m/s. The prediction transverse elastic modulus was $E_T = 5.1 \pm 0.7$ GPa which is in good agreement with AFM nanoscale indentation results (Wagner et al. 2011). This agreement illustrates the possibilities of developing nanoscale indentation models to predict the elastic behavior of individual cellulose crystals.

Acknowledgments The authors would like to thank Dr. Joseph Jakes of the USDA-Forest Service-Forest Product Laboratory for his insights on nanoscale indentation. The authors are grateful to financial support for this research provided by the Forest Products Laboratory under USDA grant: 11–JV–11111129–087 – Atomic-Scale Modeling of Cellulose Nanocrystals and for CNCs material, and Air Force Office of Sponsored Research grant: FA9550–11–1–0162.

References

Bergenstråle M, Berglund LA, Mazeau K (2007) Thermal response in crystalline Iβ cellulose: a molecular dynamics study. J Phys Chem B 111(30):9138–9145

Cousins SK, Brown RM (1995) Cellulose I microfibril assembly: computational molecular mechanics energy analysis favours bonding by van der Waals forces as the initial step in crystallization. Polymer 36(20):3885–3888

Diddens I, Murphy B, Krisch M, Müller M (2008) Anisotropic elastic properties of cellulose measured using inelastic X-ray scattering. Macromolecules 41:9755–9759

Eichhorn SJ, Davies GR (2006) Modelling the crystalline deformation of native and regenerated cellulose. Cellulose 13:291–307

Iwamoto S, Kai W, Isogai A, Iwata T (2009) Elastic modulus of single cellulose microfibrils from tunicate measured by atomic force microscopy. Biomacromolecules 10:2571–2576

Jakes JE, Frihart CR, Beecher JF, Moon RJ, Stone DS (2008) Experimental method to account for structural compliance in nanoindentation measurements. J Mater Res 23(4):1113–1127

Jakes JE, Frihart CR, Beecher JF, Moon RJ, Resto PJ, Melgarejo ZH, Suárez OM, Baumgart H, Elmustafa AA, Stone DS (2009) Nanoindentation near the edge. J Mater Res 24(3): 1016–1031

Kroon-Batenburg LMJ, Kroon J (1997) The crystal and molecular structures of cellulose I and II. Glycoconj J 14:677–690

Lahiji RR, Xu X, Reifenberger R, Raman A, Rudie A, Moon RJ (2010) Atomic force microscopy characterization of cellulose nanocrystals. Langmuir 26(6):4480–4488

Matsuo M, Sawatari C, Iwai Y, Ozaki F (1990) Effect of orientation distribution and crystallinity on the measurement by X-ray diffraction of the crystal lattice moduli of cellulose I and II. Macromolecules 23(13):3266–3275

Mattsson TR, Lane JMD, Cochrane KR, Desjarlais MP, Thompson AP, Pierce F, Grest GS (2010) First-principles and classical molecular dynamics simulation of shocked polymers. Phys Rev B 81:054103

McAllister QP, Gillespie JW, VanLandingham MR (2012) Evaluation of the three-dimensional properties of Kevlar across length scales. J Mater Res, Available on CJO 28 March 2012

Moon RJ, Martini A, Nairn J, Simonsen J, Youngblood J (2011) Cellulose nanomaterials review: structure, properties and nanocomposites. Chem Soc Rev 40(7):3941–3994

Neyertz S, Pizzi A, Merlin A, Maigret B, Brown D, Deglise X (2000) A new all-atom force field for crystalline cellulose I. J Appl Polym Sci 78(11):1939–1946

Nishiyama Y (2009) Structure and properties of the cellulose microfibril. J Wood Sci 55(4):241–249

Nishiyama Y, Langan P, Chanzy H (2002) Crystal structure and hydrogen-bonding system in cellulose Iβ from synchrotron X-ray and neutron fiber diffraction. J Am Chem Soc 124(31):9074–9082

Nishiyama Y, Sugiyama J, Chanzy H, Langan P (2003) Crystal structure and hydrogen bonding system in cellulose Iα from synchrotron X-ray and neutron fiber diffraction. J Am Chem Soc (47):14300–14306

Nishiyama Y, Johnson GP, French AD, Forsyth VT, Langan P (2008) Neutron crystallography, molecular dynamics, and quantum mechanics studies of the nature of hydrogen bonding in cellulose Iβ. Biomacromolecules 9:3133–3140

Oliver WC, Pharr GM (1992) An improved technique for determining hardness and elastic modulus using load and displacement sensing indentation experiments. J Mater Res 7(6):1564–1583

Pakzad A, Simonsen J, Heiden PA, Yassar RS (2012) Size effects on the nanomechanical properties of cellulose I nanocrystals. J Mater Res 27:528–536

Postek MT, Vladár A, Dagata J, Farkas N, Ming B, Sabo R, Wegner TH, Beecher J (2008) Cellulose nanocrystals the next big nano-thing? In: Proceedings of SPIE 7042:704 20D–1

Postek MT, Vladár A, Dagata J, Farkas N, Ming B, Wagner R, Raman A, Moon RJ, Sabo R, Wegner TH, Beecher J (2011) Development of the metrology and imaging of cellulose nanocrystals. Meas Sci Technol 22:024005

Reiling S, Brickmann J (1995) Theoretical Investigations on the structure and physical properties of cellulose. Macromol Theory Simul 4:725–743

Rusli R, Eichhorn SJ (2008) Determination of the stiffness of cellulose nanowhiskers and the fiber-matrix interface in a nanocomposite using raman spectroscopy. Appl Phys Lett 93:033111

Sakurada I, Nukushina Y, Ito T (1962) Experimental determination of the elastic modulus of crystalline regions in oriented polymere. J Polym Sci 57:651–660

Sakurada I, Ito T, Nakamae K (1964) Elastic moduli of polymer crystals for the chain axial direction. Makromol Chem 75(1):1–10

Samir MASA, Alloin FA, Dufresne A (2005) Review of recent research into cellulosic whiskers, their properties and their application in nanocomposite field. Biomacromolecules 6:612–626

Sturcová A, Davies GR, Eichhorn SJ (2005) Elastic modulus and stress-transfer properties of tunicate cellulose whiskers. Biomacromolecules 6(2):1055–1061

Tanaka F, Iwata T (2006) Estimation of the elastic modulus of cellulose crystal by molecular mechanics simulation. Cellulose 13:509–517

Tashiro K, Kobayashi M (1991) Theoretical evaluation of three-dimensional elastic constants of native and regenerated celluloses: role of hydrogen bonds. Polymer 32(8):1516–1526

Wagner R, Raman A, Moon RJ (2010) Transverse elasticity of cellulose nanocrystals via atomic force microscopy. In: 10th international conference on wood & biofiber plastic composites and cellulose nanocomposites symposium, May 11–13, Madison, WI, USA, pp 309–317

Wagner R, Moon RJ, Pratt J, Shaw G, Raman A (2011) Uncertainty quantification in nanomechanical measurements using the atomic force microscope. Nanotechnology 22(45):455703

Wu X, Moon RJ, Martini A (2011) Calculation of single chain cellulose elasticity using fully atomistic modeling. TAPPI J 10(4):37–43